Silver-based catalytic materials for the simultaneous removal of soot and NO_x

Lidia Castoldi[a,*], Eleonora Aneggi[b], Roberto Matarrese[a], Rossella Bonzi[a], Jordi Llorca[c], Alessandro Trovarelli[b,*], Luca Lietti[a]

[a] *Politecnico di Milano, Dipartimento di Energia, via La Masa 34, 20156 Milano, Italy*
[b] *Università di Udine, DCFA, via Cotonificio 108, 33100 Udine, Italy*
[c] *Institute of Energy Technologies and Centre for Research in NanoEngineering, Universitat Politècnica de Catalunya, Diagonal 647, 08028 Barcelona, Spain*

Received 5 November 2014
Received in revised form 5 February 2015
Accepted 9 February 2015
Available online 26 March 2015

1. Introduction

Diesel engines are becoming very popular due to their high efficiency and low operating costs; moreover diesel engines show higher durability than gasoline ones. However, a major environmental problem associated with diesel is the emission of particulate matter (PM) from the exhaust together with NO_x, CO and unburned hydrocarbons (HC) which has led to serious environmental problems. PM, which mostly consists of carbonaceous soot and soluble organic fraction (SOF) of hydrocarbons that have condensed on the soot, is a potential carcinogen, and reducing its volume will be an important target in the forthcoming years. One of the principal solution to reduce emissions from diesel exhausts is the catalytic oxidation technique; indeed, CO and HC oxidation can be easily accomplished with a diesel oxidation catalyst (DOC) [1] based on noble metals (e.g. Pt, Pd), but simultaneous reduction of NO_x and soot requires complex abatement strategies [2].

Among the NO_x abatement technologies, the NH_3/urea selective catalytic reduction (SCR) and the NO_x storage–reduction (NSR), also quoted as lean NO_x trap (LNT), are promising NO_x control strategies. On the other hand, diesel particulate filters (DPF) are used to remove soot particles from the exhaust stream [3–6]. These filters usually consist of wall-flow monoliths, that is, honeycomb-like structures with 50% of the channels plugged at the gas entry side and the remaining channels plugged at the exit. The gas stream enters the filter through the open channels and it is forced to pass through the porous walls where the soot particles are trapped. DPF filters must be regenerated by soot combustion in order to avoid pressure drop in the exhaust and several commercially available technologies have been designed for this purpose [7].

Catalytic oxidation of the soot is one of the most favored solutions proposed for the regeneration of DPF. The use of a large number of catalytic materials has been documented in last decade [8,9], including formulations with noble metals (mainly Pt), alkaline

* Corresponding authors.
E-mail addresses: lidia.castoldi@polimi.it (L. Castoldi), alessandro.trovarelli@uniud.it (A. Trovarelli).

and alkaline earth metals or transition metals that can accomplish redox cycles (V, Mn, Co, Cu, Fe, etc.), and internal transition metals [10]. The challenges are mainly related to their low temperature activity and long-term thermal and chemical stability.

The use of ceria (CeO_2) either alone or in combination with other oxides for the oxidation of carbon particles has been reported by several authors [11,12]. It is believed that the mechanism of action is based on its redox activity and its ability to deliver oxygen from the lattice to the carbon soot particle in a wide temperature region. In several studies the key role of surface area/composition and oxygen storage capacity was taken into account and a strong relationship between oxygen storage/redox capacity and soot combustion activity was found [13]. In order to enhance soot oxidation performances of ceria, a growing number of studies have specifically investigated the effect of addition of silver [14–19]. The presence of highly reducible surface oxygen at silver–ceria interface was reported to positively affect the soot oxidation activity of Ag/CeO_2 catalysts under either oxygen or inert atmosphere [18] and the beneficial effect of silver and its ability to alter the redox of ceria and the formation of active oxygen and peroxo species was also established from a theoretical point of view [17]. Aneggi et al. [15] showed that addition of Ag resulted in active soot oxidation catalysts either on ceria and other supports like Al_2O_3 or ZrO_2; difference in activity were explained by the tendency of the different supports in stabilizing silver in the metallic or oxide state. Formation of active oxygen species on silver can be at the origin of its good performances even in the presence of other supports [15,18–20].

Technologies for the simultaneous removal of soot and NO_x are also suggested. A possibility is to reduce NO_x with soot, while soot is being oxidized. This approach has been investigated e.g. by Kureti et al. [21] over Fe_2O_3-based catalysts and by Krishna et al. [22] over CeO_2-based catalysts.

A different solution is the DPNR (diesel particulate NO_x reduction) technology that has been proposed by Toyota [23]. This technology is available for both diesel and direct-injection (DI) lean gasoline engines. The soot combustion is in this case accomplished on the NSR (NO_x storage and reduction) catalyst during the NO_x removal [24,25]. NSR catalysts consist of a high surface area support (e.g. γ-alumina), a noble metal (Pt), and an alkaline or earth-alkaline metal oxide (e.g. K, Ba, Sr) which presents a high NO_x storage capacity. The NO_x removal mechanism in the DPNR system is that occurring on LNT catalysts [26–29]. These catalytic systems work under cyclic conditions, alternating a lean phase during which the NO_x produced by the engine are adsorbed on the alkaline or earth-alkaline metal oxide component (with nitrite/nitrate species formation depending on the temperature [30]), and a short rich phase, during which the stored nitrate species are reduced to nitrogen. Soot abatement occurs under lean conditions thanks to the NO_x storage phase and to oxygen excess in the exhaust gas; soot removal is however claimed to occur during the rich phase as well [24].

The potential utilization of a typical $Pt–Ba/Al_2O_3$ NSR catalyst for the simultaneous removal of soot and NO_x was investigated by some of us in previous works and compared with that of a Pt/Al_2O_3 sample [31–33]. It was found that the $Pt–Ba/Al_2O_3$ catalyst was able to remove both soot and NO_x simultaneously, while the Pt/Al_2O_3 catalyst performed the soot oxidation effectively but was incapable of significantly removing the gas phase NO_x. Moreover, we observed that the presence of soot in the catalytic bed led to a decrease in the NO_x storage capacity (NSC) of the catalysts. However, the loss of NSC measured in the presence of carbon varied as a function of the catalyst composition [10]. Soot oxidation activity and the deactivation of Al_2O_3-supported NSR catalysts containing Pt and K were also studied [34,25,35]. The recorded results pointed out that the $Pt–K/Al_2O_3$ catalyst was more active than $Pt–Ba/Al_2O_3$ due to the higher mobility of the NO_x species adsorbed on potassium compared to those adsorbed on barium. However, $Pt–K/Al_2O_3$ catalyst showed a partial deactivation upon aging with repeated NO_x storage–reduction cycles and soot combustion (i.e. decreased NO_x storage capacity and also lower soot oxidation activity) [36].

In this paper, we propose to combine the potential of silver-supported catalysts in the soot combustion with the NO_x storage capacity of alkaline-earth containing catalysts. For this purpose, Ag-based catalysts supported on Al_2O_3, CeO_2, and ZrO_2 have been prepared, and doped with Ba or Sr as storage components. The soot oxidation activity has been tested at first by means of temperature programmed oxidation (TPO). Then the performances of such catalysts in the removal of NO_x and of NO_x + soot have been studied.

2. Experimental

2.1. Catalysts preparation and characterization

The Ag–Ba/MO (MO = CeO_2, ZrO_2, Al_2O_3) and $Ag–Sr/CeO_2$ catalysts were prepared by incipient wetness impregnation of ceria, zirconia and alumina (obtained from Grace Davison) with aqueous solutions of silver nitrate, barium acetate and strontium nitrate (purchased from Aldrich), respectively, in order to obtain catalysts with 5 wt% loading of Ag and 10 wt% loading of Ba or Sr. After impregnation, the catalysts were dried at 100 °C overnight and calcined under air at 500 °C for 3 h.

Textural characteristics were measured according to the B.E.T. method by N_2 adsorption–desorption at −196 °C, using a Tristar 3000 gas adsorption analyzer (Micromeritics). Structural features of the catalysts were investigated by powder X-ray diffraction analysis (XRD). Diffractograms were recorded on a Philips X'Pert diffractometer (equipped with a real time multiple strip detector) operated at 40 kV and 40 mA with Ni-filtered Cu-Kα radiation, using a step size of 0.02° and a counting time of 40 s per angular abscissa in the range 20°–80°. The Philips X'Pert HighScore software was used for phase identification.

For high-resolution transmission electron microscopy studies (HRTEM), a JEOL JEM 2010F electron microscope equipped with a field emission gun was used working at an accelerating voltage of 200 kV under bright field mode. Samples were dispersed in ethanol in an ultrasonic bath and a drop of supernatant suspension was poured onto a holey carbon coated grid and dried completely before measurements.

Surface characterization was done with X-ray photoelectron spectroscopy (XPS) on a SPECS system equipped with an Al anode XR50 source operating at 150 mW and a Phoibos 150 MCD-9 detector. The pass energy of the hemispherical analyzer was set at 25 eV and the energy step was set at 0.1 eV. Charge stabilization was achieved by using a SPECS Flood Gun FG 15/40. The sample powders were pressed to self-consistent disks. Data processing was performed with the CasaXPS program (Casa Software Ltd., UK). The binding energy (BE) values were referred to the Ce 3d U‴ peak at 916.8 eV.

Temperature-programmed reduction (TPR) experiments with an AutoChem II 2920 instrument (Micromeritics) have been used to measure the redox behavior of the catalytic materials. Samples (50–60 mg) were heated from room temperature to 800 °C at a constant rate (10 °C/min) in a U-shaped quartz reactor, under a flowing hydrogen/argon mixture (30 ml/min, 4.6% H_2 in N_2) while monitoring the hydrogen consumption with a TCD detector. The outlet gas composition was also followed by an on line quadrupole mass-spectrometer (Omnistar, Balzers Instruments).

2.2. Catalytic tests and methods

The catalytic activity for the combustion of soot was determined from peak-top temperature (T_p) during temperature programmed

oxidation (TPO) experiments of catalyst-soot mixtures. Printex U (Evonik-Degussa) was used as model soot, which is widely used as a model particulate matter [37] and whose properties are well described in the literature [38].

A soot/catalyst weight ratio of 1:20 was used. The mixture has been obtained by mixing each catalyst with soot with a spatula for 10 min realizing a so-called loose contact [39], which indeed is similar to the contact that arises during practical conditions. It is worth of note that the selected soot/catalyst ratio is very common in laboratory tests and, according to literature indications, it allows a correct investigation of the reactivity of soot oxidation catalysts [11,40].

In the TPO measurements, 20 mg of the above mixture were heated at a constant rate (10 °C/min) in a quartz reactor under NO/O_2 gas flow (10% O_2 (v/v) + 500 ppm NO, balance N_2; total flow 0.5 l/min). The catalyst temperature was measured by a chromel–alumel thermocouple, located on the catalyst bed. During the catalyst heating, no anomalous exotherms have been observed (i.e. rapid and uncontrolled increase of the temperature), suggesting the lack of relevant temperature gradients within the catalyst bed and within the catalyst and the gas phase. As a matter of fact, reproducibility of results was verified by running several TPO experiments on similar samples and the results in terms of T_p were always within ±3 °C. The outlet gas composition (i.e. CO, CO_2, NO and NO_2) was measured by FT-IR gas analyzers (MultiGas 2030, MKS).

The reactivity tests for the removal of NO_x and then for the simultaneous removal of NO_x and soot were performed in a micro flow-reactor apparatus consisting of a quartz tube reactor (7 mm i.d.) connected to a mass spectrometer (QMS 200, Pfeiffer Vacuum), a micro-GC (R3000, SRA) and an FT-IR analyzer (MultiGas 2030, MKS) for the on-line analysis of the outlet gases (NO, NO_2, N_2, H_2, O_2, CO, CO_2, N_2O and NH_3). 60 mg of catalyst was used in each run. Prior the catalytic activity runs, the catalyst (without soot) has been conditioned by performing a temperature programmed desorption (TPD) experiment followed by some storage/regeneration cycles according to the ICSC procedure described below. TPD has been carried out from room temperature up to 500 °C (10 °C/min) in He and holding at this temperature 20 min. Then the temperature has been decreased to 350 °C and isothermal concentration step change (ICSC) experiments have been performed by imposing a rectangular step feed of NO (1000 ppm) + 3% (v/v) O_2 in flowing He (lean phase). When catalyst saturation has been reached, the NO and O_2 concentrations have been stepwise decreased to zero, and a He purge at the same temperature (350 °C) has been performed. This leads to the desorption of weakly adsorbed NO_x species. After the He purge, catalyst regeneration (rich phase) has been carried out with H_2 (4000 ppm) in flowing He. Conditioning lasted until a reproducible behavior was obtained; this typically required 3–4 adsorption/reduction cycles. After catalyst conditioning, the $DeNO_x$ activity of Ag–Ba/MO (MO = CeO_2, ZrO_2, Al_2O_3) and Ag–Sr/CeO_2 catalysts has been tested with typical ICSC run at 350 °C in the absence of soot.

The $DeNO_x$–DeSoot activity has been tested for the same catalysts using 66 mg of soot–catalyst loose mixture (corresponding to 59.4 mg of the bare catalyst and 6.6 mg of soot, i.e. soot loading (w_{soot}/w_{cat}) near 11%) and performing seven storage–reduction cycles and subsequently oxidizing the residual soot by temperature programmed oxidation (TPO) in 3% (v/v) O_2 in He from 350 °C up to 750 °C (10 °C/min).

Pt–Ba/Al_2O_3 (1/20/100, w/w) model catalyst has been also considered for comparison purpose; details of catalyst preparation and characterization are reported elsewhere [41,42]. ICSC experiments similar to that already described have been performed over this model catalyst as also reported in previous studies [31,34].

Table 1
Composition and BET surface areas of the supports and of the silver-supported catalysts.

Sample	SA (m^2/g)
CeO_2	49
ZrO_2	59
Al_2O_3	180
Ag(5%)–Ba(10%)/CeO_2	31
Ag(5%)–Ba(10%)/ZrO_2	38
Ag(5%)–Ba(10%)/Al_2O_3	144
Ag(5%)–Sr(10%)/CeO_2	20

3. Results and discussion

3.1. Structural and morphological characterization of materials

Table 1 summarizes composition and BET surface areas of the supports and of the silver-supported catalysts. The addition of silver and alkaline-earth metals results in a drop of surface area at the loadings used in this study. This is typically observed upon addition to high-surface area supports of oxides possessing high specific weight and low porosity [43,44] and the effect is more pronounced at high loadings.

The structural and morphological characteristics of the catalysts were studied by XRD, HRTEM, XPS, TG, and TPR measurements. Fig. 1 shows the X-ray diffraction profiles of barium- and strontium-doped catalysts. In the case of barium-doped materials, peaks belonging to the supports (CeO_2, ZrO_2 and Al_2O_3) are clearly observed; in addition, the presence of signals at $2\theta = 38.1°$, 44.3° and 64.5° indicates formation of metallic silver. XRD experiments reveal also the presence of orthorhombic barium carbonate whereas no crystalline BaO is observed (with exception of Ag–Ba/Al_2O_3 where a small diffraction signal due to BaO has been detected) in agreement with several studies [45-47]. The weak intensities of $BaCO_3$ peaks indicate a low crystallization degree of the carbonate crystallites on the oxides supports. Similarly, in Ag–Sr/CeO_2 catalyst, signals due to metallic Ag and to $SrCO_3$ are observed, in addition to the peaks due to the support; no evidence for the presence of Ag_2O crystallites was obtained.

HRTEM analysis of as prepared catalysts was also used with the aim to elucidate the morphology and distribution of the different species present, and the results are reported in Figs. 2 and 3. Fig. 2A and B shows representative images of the Ag–Ba/CeO_2 catalyst. The sample contains well-dispersed silver particles corresponding to

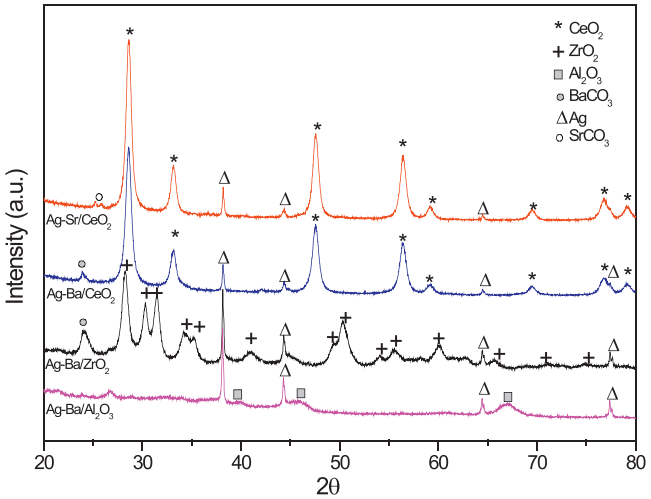

Fig. 1. X-ray diffraction profiles of Ag–Ba/MO (MO = CeO_2, ZrO_2, Al_2O_3) and Ag–Sr/CeO_2 catalysts (*CeO_2; +ZrO_2; ■Al_2O_3; ●$BaCO_3$; △Ag; ○ $SrCO_3$).

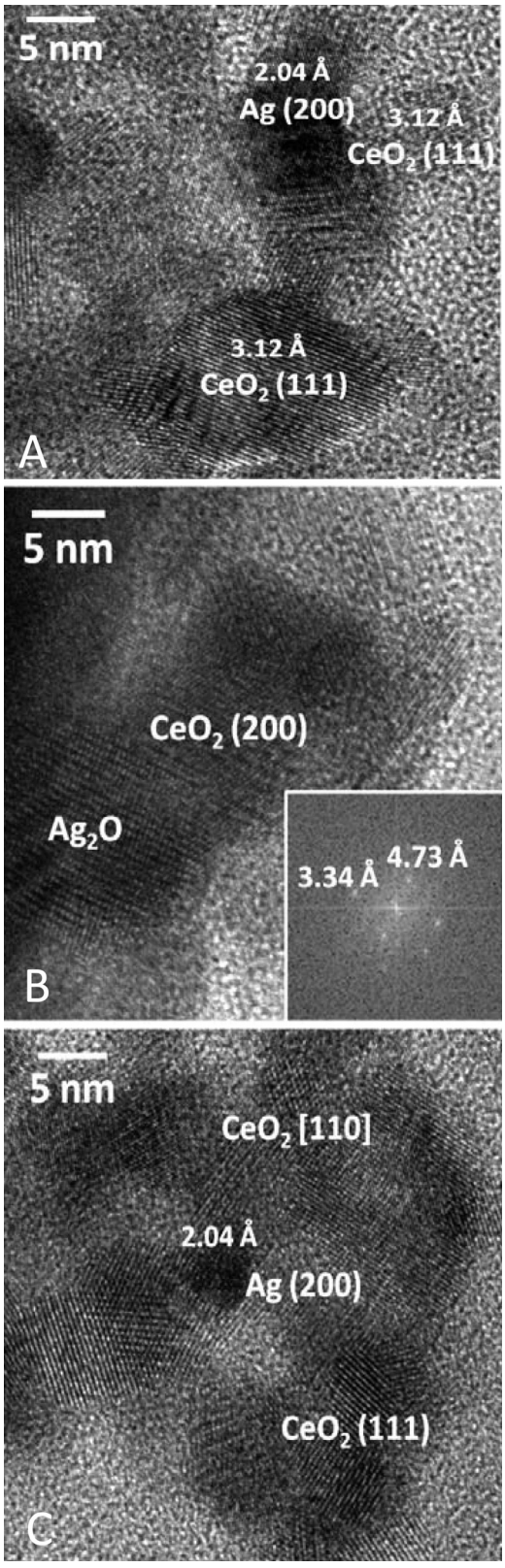

Fig. 2. HRTEM images of Ag–Ba/CeO_2 (A and B) and Ag–Sr/CeO_2 (C).

both metallic Ag and Ag_2O (the latest more evident in Fig. 2B); metallic Ag nanoparticles diameter ranges about 5 nm and Ag_2O nanoparticles about 10–15 nm. The dispersion of both Ag and Ag_2O is good. Ag nanoparticles are identified by lattice fringes at 2.04 Å which correspond to the (2 0 0) crystallographic plane of metallic Ag (Fig. 2A). In the FT image in Fig. 2B, the spots at 3.34 and 4.73 Å correspond to the (1 1 0) and (1 0 0) crystallographic planes of Ag_2O, respectively. It is worth noticing that metallic Ag is more abundant than Ag_2O; this is likely at the origin of the fact that X-ray diffraction data reveal only the presence of metallic Ag, which might be due to the low concentration of Ag_2O particles. Ceria crystallites are observed, ranging about 10–20 nm in size and in close contact to both metallic Ag and Ag_2O; several ceria crystallites are identified by their characteristic lattice spacing. Fig. 2C shows an image of Ag–Sr/CeO_2 sample, which is constituted by ceria crystallites of about 10–15 nm and a good dispersion of metallic Ag nanoparticles of about 5 nm. This is quite similar to the Ba-containing sample; however, no Ag_2O has been detected.

In Fig. 3A images of Ag–Ba/ZrO_2 catalyst is reported. The sample contains crystalline ZrO_2 particles of about 20–30 nm, and in addition only metallic Ag crystallites have been observed. The lattice fringes at 2.04 Å at 90° in the FT image indicate that the Ag crystallite is oriented along the crystallographic direction [48]. Finally, the Ag–Ba/Al_2O_3 catalyst (Fig. 3B) contains a broad distribution of Ag metal particles ranging from 5 up to 50 nm in size; accordingly, the dispersion of Ag in Al_2O_3 is therefore poor compared to CeO_2 and ZrO_2.

The surface composition, the chemical states of the elements and their nature were examined by the XPS technique. The binding energies (eV) of the most intense photoelectron Ba $3d_{5/2}$, Ag $3d_{5/2}$, Ce $3d_{5/2}$, O 1s, Zr $3p_{3/2}$, Al 2p, and Sr $3p_{3/2}$ peaks of calcined catalysts, as well as atomic concentration (%) and atomic ratios are compiled in Table 2.

Surface concentration of elements confirms the lowest dispersion of the Ag–Ba/Al_2O_3 sample in accordance with HRTEM. In the deconvolution of the Ag 3d signal, fitting of the spectra can be obtained with only one doublet indicating that a single species constitutes most of the Ag in the samples. However, the binding energy values of the Ag 3d signal do not allow distinguishing between Ag and Ag_2O. This is in accordance with the presence of metallic Ag only in samples containing ZrO_2 and Al_2O_3 and it is still compatible with the presence of small amount of Ag_2O with Ba containing ceria-based support, in accordance with XRD results. In addition, Ag–Sr/CeO_2 compared to Ag–Ba/CeO_2, shows that the amount of Sr at the surface is double than that of Ba, indicating a superior dispersion of strontium.

Fig. 4(A and E) shows the temperature programmed reduction profiles of Ag–Ba/MO (MO = CeO_2, ZrO_2, Al_2O_3) and Ag–Sr/CeO_2 catalysts, respectively; inset (B) shows the TPR of the bare supports. The reduction of bare ceria shows two main peaks, one at low temperature (near 450 °C) due to surface reduction and the second above 700 °C correlated to bulk Ce^{4+} reduction [49]; the TPR profiles of the other supports (also reported in the inset (B)) show a flat profile, in line with their reduction behavior under TPR conditions [50,51]. For all the catalysts, it is possible to recognize two major broad regions for hydrogen consumption, one at low temperature, centered at around 150–200 °C, and one at high temperature, at around 650–700 °C. In all cases, reduction peaks at low temperature are correlated to the formation of methane originating from reduction of carbonate species and likely due to a non-complete decomposition during the calcination (insets (C) and (F) show the CH_4 production in the case of CeO_2-based catalysts). The higher intensity of low-temperature peak in Ag–Sr/CeO_2 compared to Ba-doped catalysts can be associated to the higher surface Sr dispersion, as evidenced by XPS analysis, which might lead to a higher amount of surface carbonates. The presence of surface Ba and Sr might be also responsible for the disappearance of the surface reduction peak of ceria. Note that in the case of ceria-supported catalysts a portion of the low temperature reduction peak might be associated to reduction of surface cerium species and reduction of small quantities of Ag_2O [15].

Table 2
Binding energies (eV) of the most intense photoelectron O 1s, Ag $3d_{5/2}$, Ba $3d_{5/2}$, Sr $3p_{3/2}$, Ce $3d_{5/2}$, Zr $3p_{3/2}$, Al 2p, and peaks of calcined catalysts, as well as atomic concentration (%) and atomic ratios.

Sample	Peaks	Binding energy (eV)	Atomic concentration (%)	Ag/Ce, Zr, Al atomic ratio	Ba, Sr/Ce, Zr, Al atomic ratio
Ag–Ba/CeO_2	O 1s	529.0	60.7		
	Ag $3d_{5/2}$	367.8	2.5	0.078	
	Ba $3d_{5/2}$	780.0	4.9		0.154
	Ce $3d_{5/2}$	882.1	31.9		
Ag–Ba/ZrO_2	O 1s	529.5	71.4		
	Ag $3d_{5/2}$	367.9	2.2	0.101	
	Ba $3d_{5/2}$	780.0	4.7		0.217
	Zr $3p_{3/2}$	332.2	21.7		
Ag–Ba/Al_2O_3	O 1s	530.4	62.4		
	Ag $3d_{5/2}$	367.8	0.8	0.023	
	Ba $3d_{5/2}$	779.9	1.9		0.053
	Al 2p	73.5	34.9		
Ag–Sr/CeO_2	O 1s	529.2	65.3		
	Ag $3d_{5/2}$	368.2	1.45	0.057	
	Sr $3p_{3/2}$	268.9	7.9		0.310
	Ce $3d_{5/2}$	882.0	25.4		

Peaks at higher temperature are associated to traces of methane formation and desorption of carbonates and nitrates/nitrites as CO_2 and NO respectively (insets (D) and (G) in Fig. 4); in the case of ceria, peaks at high temperature include hydrogen consumption for reduction of residual surface Ce^{4+} and bulk CeO_2 [49].

3.2. Soot oxidation activity

Fig. 5A and B summarizes the results of the soot combustion experiments (TPO) carried out in $NO/O_2/N_2$ atmosphere. In Fig. 5A are reported the two most important parameters usually used to compare the TPO results, namely the onset temperature (gray column) and the peak temperature (black column). The first is evaluated in correspondence of 20 ppm of CO_2 produced by the oxidation process, while the latest corresponds to the maximum production of CO_2.

All the investigated catalysts are active in soot oxidation (Fig. 5A) with a remarkable decrease of oxidation onset temperature compared to uncatalyzed reaction; the catalytic oxidation is highly selective to CO_2 (only negligible amount of CO were formed), whereas the uncatalyzed reaction produces CO along with CO_2. The higher oxidation temperature (i.e. the lowest oxidation activity) are found with the Al_2O_3-based catalyst, and are likely related to the low Ag dispersion observed over these materials, while Ba and Sr do not seem to strongly influence the activity. Moreover, in all cases the oxidation of soot is complete at the end of the experiment. Note that the CO_2 evolution profiles have regular shape with a maximum near 460–470 °C and return to background level before the end of the experiment. The NO_2 concentration initially increases with temperature due to the occurrence of the NO oxidation reaction; then the NO_2 concentration decreases due to its involvement in the soot oxidation and to thermodynamic reasons.

It is well known that metallic silver can form several sub-oxide species in oxidation atmosphere [52-57] and can also promote the formation of superoxide O^{2-} ions [58]; these species might assist the carbon oxidation by O_2 [15].

Also, in Fig. 5B the evolution of NO_2 concentration during the soot oxidation is reported. As it clearly appears, all the catalysts are active in the oxidation of NO to NO_2 and the onset temperature for the NO_2 evolution is observed below 250 °C, i.e. at a temperature lower than the onset temperature for soot oxidation. A correlation between the NO_2 production and the peak temperature for soot oxidation can be found. Indeed, the presence of metallic Ag can influence the rate of NO_2 formation that in turn can be transported

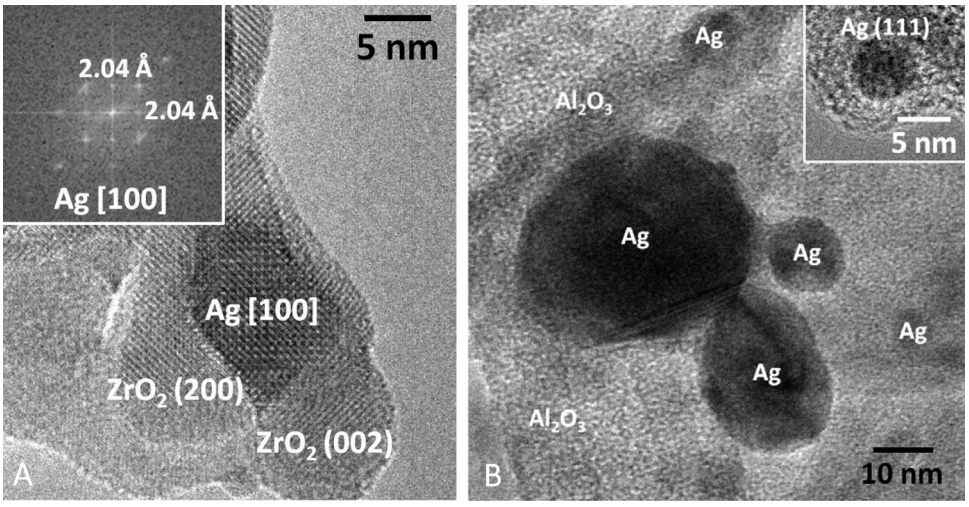

Fig. 3. HRTEM images of Ag–Ba/ZrO_2 (A) and Ag–Ba/Al_2O_3 (B).

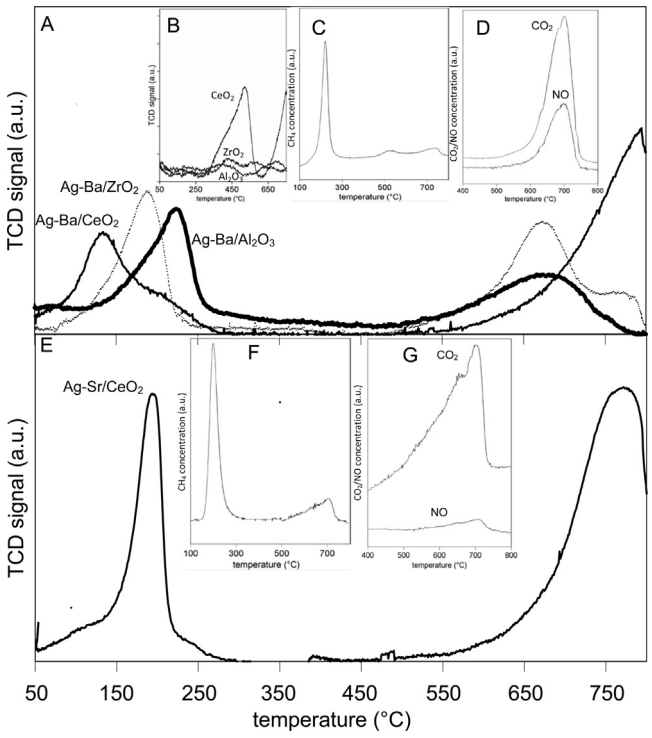

Fig. 4. (A) H_2 consumption profiles for Ag–Ba/MO (MO = CeO_2, ZrO_2, Al_2O_3) during TPR experiment. Inset (B): H_2 consumption profiles for bare supports (CeO_2, ZrO_2, Al_2O_3); inset (C): production of CH_4 for Ag–Ba/CeO_2; inset (D): evolution of CO_2/NO for Ag–Ba/CeO_2. (E) H_2 consumption profile for Ag–Sr/CeO_2 catalyst. Inset (F): production of CH_4 for Ag–Sr/CeO_2; inset (G): evolution of CO_2/NO for Ag–Sr/CeO_2.

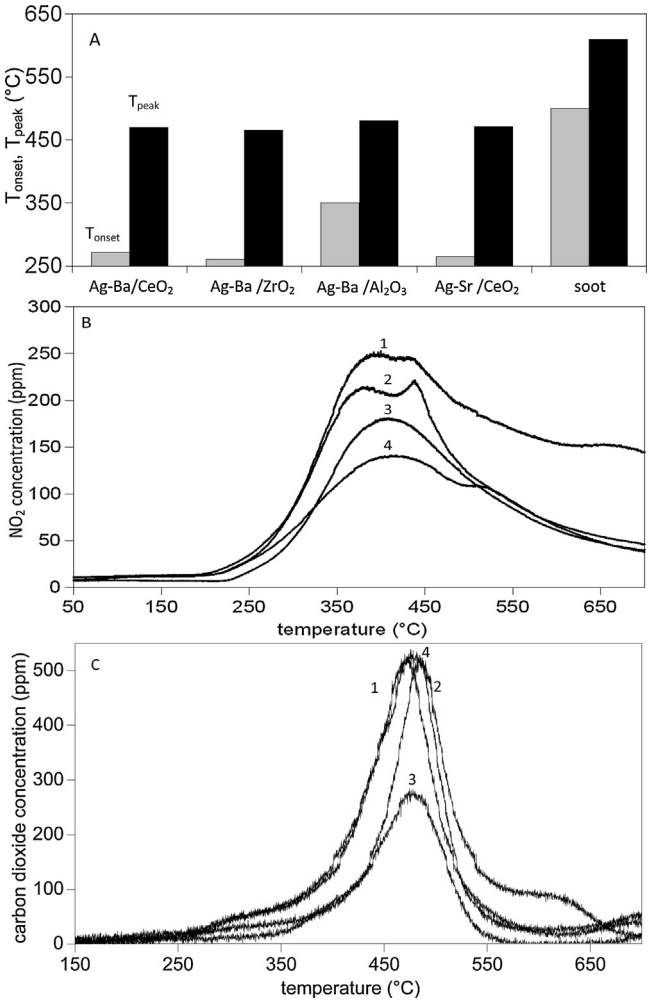

Fig. 5. (A) T_{onset} (gray column) and T_{peak} (black column) for soot combustion in NO/O_2 atmosphere; (B) NO_2 production during soot combustion in NO/O_2 atmosphere; (C) CO_2 production during soot combustion in NO/O_2 atmosphere (1, Ag–Ba/ZrO_2; 2, Ag–Ba/CeO_2; 3, Ag–Sr/CeO_2; 4, Ag–Ba/Al_2O_3).

via the gas phase over soot particles, oxidizing carbon while being reduced back to NO [59,60]. Therefore, both NO_2-assisted and O_2-promoted soot oxidation mechanisms can be observed here.

3.3. NO_x and soot removal

The $DeNO_x$ (i.e. the removal of NO_x) and the combined $DeNO_x$–DeSoot (i.e. the simultaneous removal of NO_x and soot) activity has been tested at first for the CeO_2-supported catalysts, namely Ag–Ba/CeO_2 and Ag–Sr/CeO_2, in order to elucidate the role of the storage component (i.e. of the alkaline-earth metal oxide, Ba vs. Sr). Then in the case of Ba-containing catalysts the effect of the support (i.e. CeO_2 vs. ZrO_2 and Al_2O_3) has been studied as well.

3.3.1. $DeNO_x$ activity

3.3.1.1. NO_x storage. The NO_x storage/reduction activity over the fully conditioned Ag–Ba/CeO_2 and Ag–Sr/CeO_2 catalysts in the absence of soot has been investigated at 350 °C and the results reported in Fig. 6A and B, respectively. The figure shows the NO, NO_2, NO_x (i.e. NO + NO_2) concentration profiles during the lean phase, and N_2 NO, NH_3, H_2 concentration profiles measured during the rich phase; the thermal desorption in inert atmosphere subsequent to the rich phase is also reported.

In the case of Ag–Ba/CeO_2 catalyst (Fig. 6A), NO is observed at the reactor outlet 18 s after its admission (t = 0 s), i.e. the NO breakthrough is very short. Then, the NO concentration increases with time, reaching the value of 488 ppm; at this time the NO feed is closed. Also, NO_2 is immediately observed at the reactor outlet and increases up to 454 ppm. The NO_2 production is related to the NO oxidation on Ag sites (NO + 1/2 O_2 → NO_2).

Note that the NO pulse is stopped before the NO_x concentration reached a steady level, indicating that saturation of the catalyst surface is not yet completed after 1860 s. The integral curve of stored NO_x as a function of time-on-stream is plotted in Fig. 7A. The NO_x stored at this temperature at the end of adsorption are close to 1.15×10^{-3} mol/g_{cat}, corresponding to the involvement of 78% of the overall Ba loading by assuming the formation of $Ba(NO_3)_2$ species. The exploitation of Ba sites is much higher than in the traditional Pt–Ba/Al_2O_3 catalyst where only 20–30% of Ba participates to the storage at 350 °C [61]; however in this case the participation of CeO_2 to the storage process cannot be excluded.

When the NO and O_2 inlet concentrations are switched off (t = 1860 s and 2477 s, respectively in Fig. 6A), a tail is observed in the NO_x concentration profile, due to the desorption of weakly adsorbed NO_x species [62]. The net amount of stored NO_x has been calculated by difference of the NO_x adsorbed during NO feeding and the NO_x desorbed before the regeneration phase and it is close to 9.14×10^{-4} mol/g_{cat}, corresponding to a decrease of approx. 20% of the initial NO_x loading.

In Fig. 6B the storage phase of the conditioned Ag–Sr/CeO_2 catalyst is reported. In this case, NO is immediately observed at the reactor outlet upon its admission (t = 0 s), i.e. the NO breakthrough is zero; the NO_x stored amounts up to saturation are close to 9.45×10^{-4} mol/g_{cat}, corresponding to 41% of the overall Sr loading. Notably, assuming that NO_x are stored on Sr only, the amount of stored NO_x is lower than that of the Ba-based sample. This could be explained considering the different basicity of the two alkaline

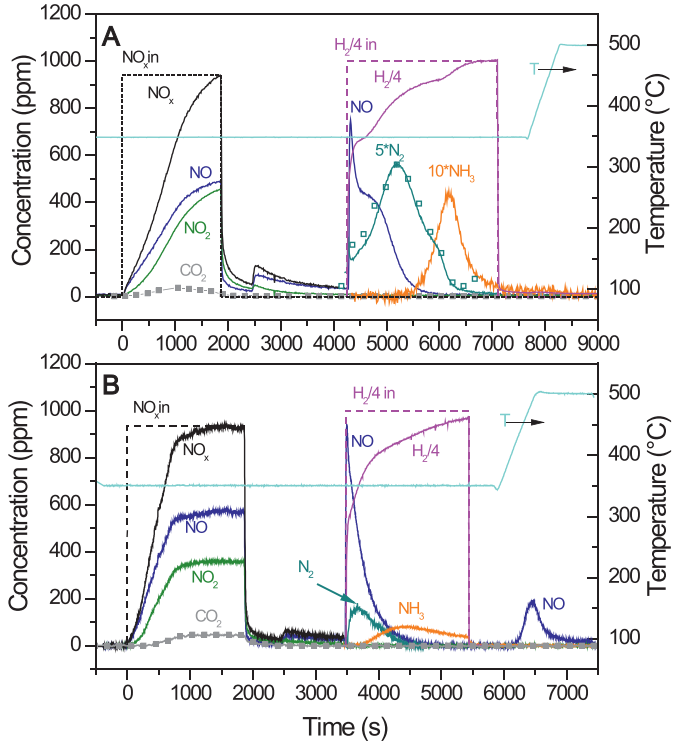

Fig. 6. Adsorption, reduction and thermal desorption phases over (A) Ag–Ba/CeO_2 catalyst; (B) Ag–Sr/CeO_2 catalyst in the absence of soot. Storage phase: 1000 ppm NO + 3% (v/v) O_2 in He at 350 °C; reduction phase: 4000 ppm H_2 in He at 350 °C; thermal desorption in He from 350 °C up to 500 °C (10 °C/min).

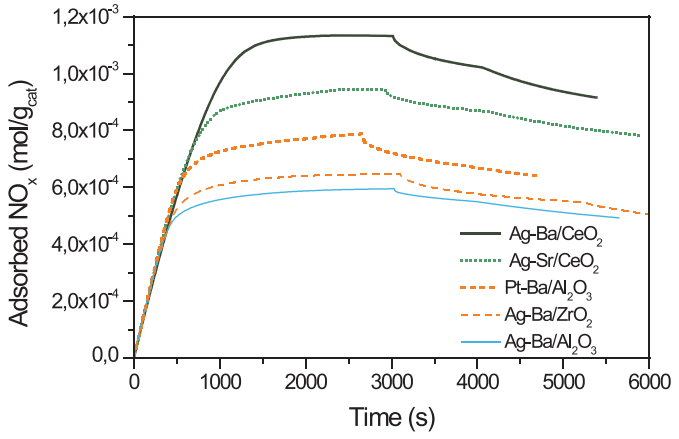

Fig. 7. Integral curves of stored NO_x vs. time in the absence of soot over Ag–Ba/CeO_2 (thick solid lines), Ag–Sr/CeO_2 (short dotted lines), Ag–Ba/ZrO_2 (dash lines) and Ag–Ba/Al_2O_3 (thin solid lines) catalysts. Integral curves of stored NO_x are also reported for Pt–Ba/Al_2O_3 model LNT catalyst (dashed line) for comparison purpose.

earth metal components (Sr vs. Ba) which is expected to affect the NO_x trapping performances, in line with literature indications [63].

Upon NO shut off, the concentrations of NO and of NO_2 decrease faster than in the case of Ag–Ba/CeO_2 system. Also, a minor NO_x desorption has been observed closing the oxygen feed gas, resulting in a storage capacity near 7.82×10^{-4} mol/g_{cat} at the end of the purge.

In Fig. 7 the integral curve of stored NO_x vs. time for the various investigated samples is shown together with that of Pt–Ba/Al_2O_3 model LNT catalyst. The LNT model catalyst exhibits a lower storage capacity than that of the two CeO_2-supported catalysts; in particular, the amount of stored NO_x increases in the order Pt–Ba/Al_2O_3 < Ag–Sr/CeO_2 < Ag–Ba/CeO_2.

In Fig. 7 the integral curves of stored NO_x for Ag–Ba/ZrO_2 and Ag–Ba/Al_2O_3 catalysts are also reported.

The CeO_2-supported catalyst shows higher storage capacity than ZrO_2- and Al_2O_3-supported systems, being the amount of NO_x stored at steady state close to 9.14×10^{-4} mol/g_{cat} for the former and near 6×10^{-4} mol/g_{cat} vs. 7.8×10^{-4} mol/g_{cat} for the latters Ag–Ba/ZrO_2 and Ag–Ba/Al_2O_3 respectively. ZrO_2- and Al_2O_3-supported catalysts instead exhibit a lower storage capacity with respect to the traditional Pt-based LNT catalyst. From Fig. 7 it also appears that, after NO/O_2 shut off, a higher desorption of stored NO_x is observed over the Ag–Ba/CeO_2 catalyst than over other two Ba-containing catalysts. It is worth to note that the low Ag dispersion in Ag–Ba/Al_2O_3 catalysts seems not to dramatically affect the performances of this catalyst, being comparable to Ag–Ba/ZrO_2 and Ag–Ba/CeO_2 systems.

3.3.1.2. Reduction of the stored NO_x. The stored NO_x are then reduced under isothermal conditions by admitting H_2 (4000 ppm) in He and the results are shown in Fig. 6A and B for Ag–Ba/CeO_2 and Ag–Sr/CeO_2 catalysts.

At 350 °C (Fig. 6A), upon the addition of H_2 (at $t = 0$ s), a huge amount of NO is immediately observed at the reactor outlet along with lower amounts of N_2 and NH_3. The H_2 consumption is not complete and its concentration slowly increases with time until the inlet value of 4000 ppm. No production of other byproducts like N_2O is observed. At the end of the reduction phase ($t = 7096$ s in Fig. 6A), a thermal desorption under inert atmosphere is carried out in order to verify the complete regeneration of the catalytic surface. Noticing, no desorption of N-containing species is observed up to 500 °C, which indicates that the NO_x stored species are all removed and that the catalytic surface is fully regenerated, as confirmed also by N-balance. Due to the great amounts of NO produced during the reduction, the selectivity to N_2 is rather low, near 37%.

Similar results have been obtained in the case of Ag–Sr/CeO_2 catalyst (Fig. 6B); the main reduction product is NO and only small amounts of N_2 and NH_3 are detected. The overall nitrogen selectivity is in this case near 22%. Moreover, during the subsequent thermal decomposition, desorption of NO is detected starting from 410 °C; this indicates that the catalyst is not fully regenerated at the end of the reduction phase at 350 °C, as confirmed also from the N-balance.

The behavior of both Ag–Ba/CeO_2 and Ag–Sr/CeO_2 catalysts is very different from that of Pt–Ba/Al_2O_3 model LNT catalyst. In the latest case, in fact, the reduction of stored species is always complete and the selectivity to N_2 is very high, near 80%, being N_2 the main product and NH_3 and NO detected in lower amounts [64].

When the Ag–Ba/ZrO_2 and Ag–Ba/Al_2O_3 catalysts are considered (data not shown), no substantial differences have been observed with respect to Ag–Ba/CeO_2 during the reduction of stored NO_x. Also in this case, the main reduction product is NO accompanied by minor amounts of N_2 and NH_3; accordingly, the selectivity to nitrogen is near 30%. The reduction is complete and all the stored NO_x are removed at the end of this phase. It is worth to note that the low selectivity to N_2 observed in all Ag-containing catalysts should be related to the low activity of Ag, whatever is the metal dispersion.

3.3.2. DeNO$_x$–DeSoot activity

Lean–rich cycles have been performed also in the presence of soot over the Ag–Ba/CeO_2 and Ag–Sr/CeO_2 catalysts in order to study the simultaneous DeNO$_x$ and DeSoot activity. Fig. 8 shows a typical sequence of lean–rich phases at 350 °C, in terms of NO, NO_2, NO_x (=NO + NO_2), CO_2, H_2, NH_3 and N_2 outlet concentration vs. time. Fig. 8A and C refer to the first cycle over Ag–Ba/CeO_2 and Ag–Sr/CeO_2 catalysts respectively, while Fig. 8B and D refers

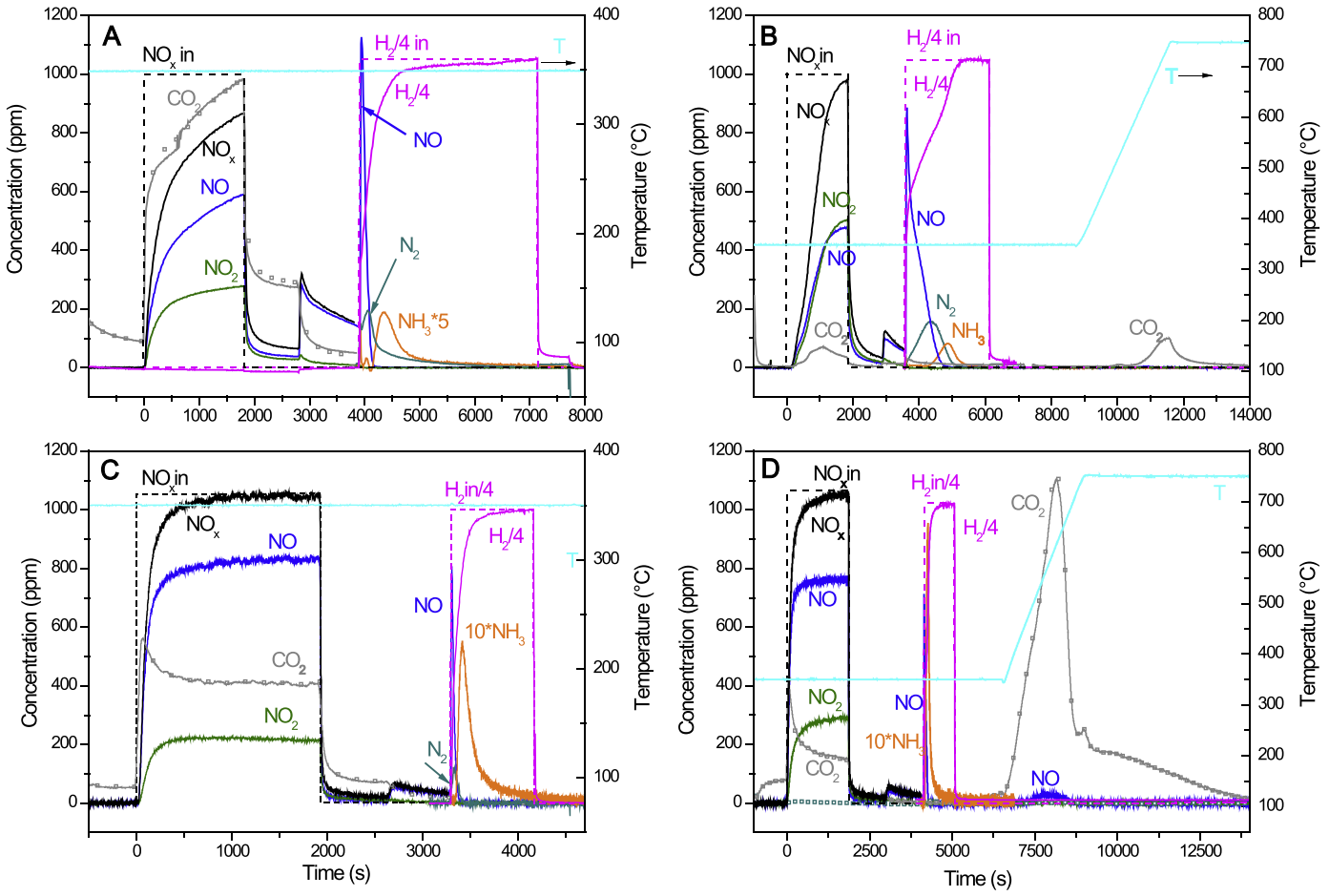

Fig. 8. Adsorption, reduction and TPO phases over (A and B) Ag–Ba/CeO_2 catalyst; (C and D) Ag–Sr/CeO_2 catalyst in the presence of soot. (A and C): first storage–reduction cycle; (B and D): seventh storage–reduction cycle and subsequent TPO. Storage phase: 1000 ppm NO + 3% (v/v) O_2 in He at 350 °C; reduction phase: 4000 ppm H_2 in He at 350 °C; TPO in 3% (v/v) O_2 in He from 350 °C up to 750 °C (10 °C/min).

to the seventh and last cycle, followed by a TPO run up to 750 °C to complete the soot combustion (see Section 2).

In the first lean–rich cycle over Ag–Ba/CeO_2 catalyst (Fig. 8A), upon NO and O_2 admission (at $t = 0$ s) the NO outlet concentration increases with time after a very short NO_x breakthrough (10 s); NO_2 formation is also observed (simultaneously to NO), due to the occurrence of the oxidation of NO by O_2 at Ag sites according to the stoichiometry of reaction (1). The outlet concentrations of both NO and NO_2 increase with time, indicating that the NO_x storage still occurs; worth to note that the storage phase is stopped before a steady state level has been reached. The amounts of NO_x that have been stored onto the catalyst surface are 2.50×10^{-5} mol/g_{cat}, lower than that measured in the absence of soot (9.14×10^{-4} mol/g_{cat}, Fig. 9A), indicating a reduced storage capacity of the catalyst in the presence of soot, as also reported in the literature [32,33,65,66].

A comparison has also been made between the NO_x stored at different residual soot loadings, i.e. in the subsequent lean–rich cycles during soot oxidation, and results are shown in Fig. 9A. It appears that the amount of soot present in the catalyst/soot mixture influences the NO_x storage behavior of the catalytic system. Accordingly, upon decreasing the residual soot loading, the NO_x storage capacity increases, approaching that of the catalyst in the absence of soot, in line with the results over Pt–Ba/Al_2O_3 catalyst and reported by some of us in a previous work [66]. The detrimental effect of the presence of soot on the performances of a Pt–Ba/Al_2O_3 LNT catalyst may be related to the decrease of the NO_2 gas phase concentration, being NO_2 involved in the soot combustion, according to reaction (1):

$$2NO_2 + C \rightarrow 2NO + CO_2 \quad (1)$$

As a matter of fact, the NO/NO_2 value increases from a value near 6 for the soot-free catalyst sample to roughly 15 in presence of soot.

In the case of Ag–Ba/CeO_2 catalyst, the NO/NO_2 ratio in the absence and in the presence of soot changes from 1.07 to 2.1 (in the first cycle where the higher amount of soot is present). Therefore, also in this case we can suppose the participation of NO_2 to soot oxidation, even if the decrease in the NO_2 concentration is less evident. Notably, oxidation by NO_2 is not likely the unique pathway for the soot oxidation; the direct participation of active oxygen from ceria and/or silver can also be invoked (as discussed below). Finally, note that reaction (1) may involve the intermediacy of CO although this species has not been observed. In fact, CO may be oxidized to CO_2 by O_2 at Ag sites and/or by NO_2.

The storage of NO_x is accompanied by the evolution of CO_2; upon NO admission, the CO_2 concentration rapidly increases (Fig. 8A) showing a maximum of 1000 ppm at the end of the storage phase. It is worth to note that its background level is not zero before NO admission, indicating that soot oxidation occurs also in the presence of O_2 alone. The presence of CO_2 in the outlet gas stream results only from soot oxidation, being CO_2 absent the inlet feed. However, the CO_2 production is not accompanied by the evolution neither of N_2 or N_2O, as reported by some authors [21,22] but

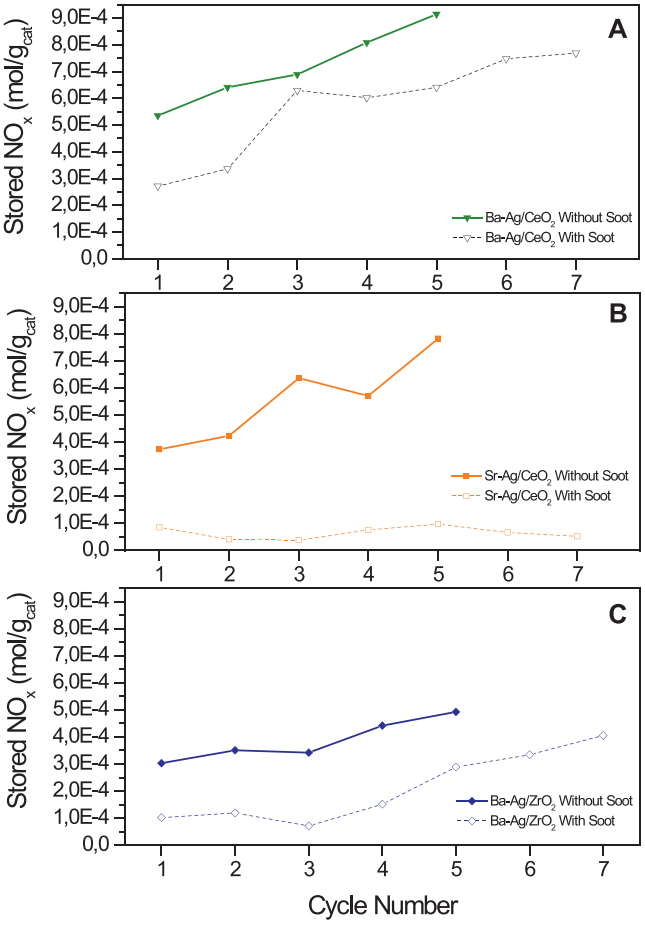

Fig. 9. Total amount of stored NO_x vs. cycle number over (A) Ag–Ba/CeO_2; (B) Ag–Sr/CeO_2 and (C) Ag–Sr/ZrO_2. Filled symbols and solid lines: absence of soot; empty symbols and dashed lines: presence of soot.

over different catalytic systems. The soot combustion activity of the Ag–Sr/CeO_2 is much higher with respect to the model Pt–Ba/Al_2O_3, as pointed out by the higher production of CO_2 detected at the reactor outlet in this case (near 1000 ppm vs. near 300 ppm for Pt–Ba/Al_2O_3 [34]).

It is worth noting that, upon the NO addition, the production of CO_2 is much higher than that expected from the stoichiometry of reaction (1). This could be explained by considering the possible "NO recycle" mechanism: in fact, similarly to the case of Pt-containing catalysts [67] it may be argued that NO which is formed in reaction (1) may be further oxidized to NO_2 by Ag metallic sites (recycling of NO to NO_2) which could substantially enhance the efficiency of soot combustion. Moreover, as described above, soot combustion is observed even in the absence of NO (i.e. in presence of only oxygen). This suggests a direct role of the catalyst (e.g. direct participation of active oxygen from ceria and/or silver) in the oxidation of soot, which is superimposed to the soot combustion activity by NO_2. Finally, as reported in previous works [32,33,66] a specific role of the stored NO_x species in the soot combustion cannot be excluded, which could contribute to the significant increase in the soot combustion. These routes operate simultaneously in the oxidation of soot, so that the relevance of each pathway cannot be determined.

Upon NO shutoff, a release of NO and NO_2 takes place with time due to the desorption of the previously stored NO_x species, and the CO_2 concentration decreases as well. Upon switching off the O_2 feed, other NO_x are also desorbed. Both desorption contributions appear to be remarkable if compared to those observed

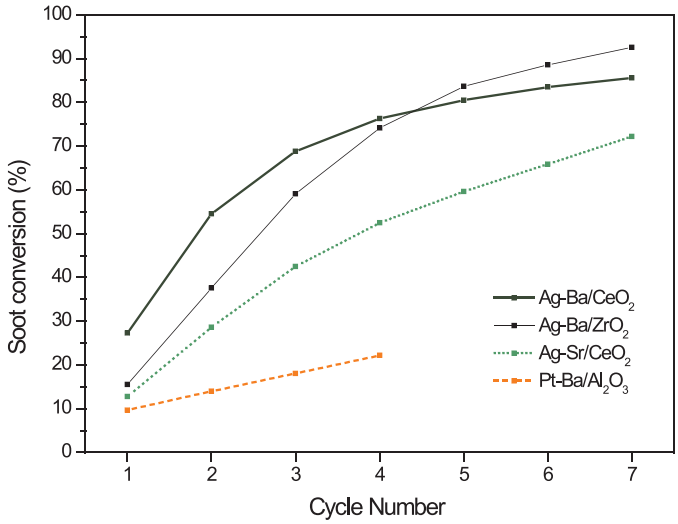

Fig. 10. Soot conversion during the lean phase as a function of the cycle number: Ag–Ba/CeO_2 catalyst (thick solid line); Ag–Ba/ZrO_2 catalyst (thin solid line); Ag–Sr/CeO_2 catalyst (dotted line); Pt–Ba/Al_2O_3 catalyst (dashed line).

in the soot-free catalyst, suggesting that soot has a destabilizing effect on the NO_x species adsorbed onto the catalytic surface; this behavior is in line with that observed in the case of Pt–Ba/Al_2O_3 LNT catalyst [32,66]. The total amount of NO_x desorbed in the presence and in the absence of soot are near 4.04×10^{-4} mol/g_{cat} and 2.33×10^{-4} mol/g_{cat}, respectively; these values correspond to 94% and 20% of the NO_x adsorbed species present onto the catalytic surface at saturation. This clearly points out to a lower stability of nitrates species in presence of soot.

The reduction of the stored NO_x has also been analyzed. Reduction has been carried out at the same temperature (350 °C) by admission of H_2 step (4000 ppm) in He. The results, reported in Fig. 8A in terms of H_2, NO, CO_2 and N_2, NH_3 outlet concentrations as a function of time, point out that the reduction of the NO_x adsorbed species in the presence of soot does not show significant differences with respect to the soot-free catalyst (compare Fig. 6A). Also in this case H_2 is immediately observed at the reactor outlet; its concentration increases with time, reaching the steady state level of inlet concentration. NO represents the main reduction product, along with minor amounts of N_2 and NH_3. No release of other byproducts like N_2O is observed; the selectivity to N_2 is near 45%.

The data described above clearly indicate that the Ag–Ba/CeO_2 catalyst is able to simultaneously store/reduce NO_x and oxidize soot. Considering the whole sequence of the seven NO_x storage–reduction cycles (Fig. 8A and B), it appears that the behavior of the catalytic system is affected by the residual soot loading. Indeed, the NO_x breakthrough progressively increases during the lean/rich sequence (compare Fig. 8A with B) moving from the first to the seventh cycle, respectively, i.e. upon increasing the soot conversion from 27% (w/w) to 85% (w/w). The increase in the dead time is accompanied by an increase of the amount of NO_x stored during the lean phase, from 2.50×10^{-4} mol/g_{cat} for the first cycle to 7.52×10^{-4} mol/g_{cat} for the seventh cycle (Fig. 9A), near to that of the catalyst in the absence of soot. Note that also the NO/NO_2 ratio changes during soot oxidation, moving from 2.17 in the first cycle to 0.9 in the seventh, very close to the value recorded in the absence of soot (compare Fig. 6A with Fig. 8A and B).

Fig. 10 shows the soot conversion during the lean phases as a function of the cycle number, estimated from the amounts of evolved CO_2. In the case of Ag–Ba/CeO_2 catalyst (solid line) during the lean phase of the first cycle, roughly 27% of the initial soot loading (6.6 mg of soot) is oxidized, which increases up to 86% during

the seventh cycle. At the end of the sequence the residual soot loading is near 14% (w/w). In fact, the CO_2 concentration measured at the end of the lean phase decreases from 980 ppm of the first cycle to 70 ppm of the seventh cycle, indicating a progressive decrease of the rate of soot combustion. These results are in line with the data collected on the Pt–Ba/Al_2O_3 LNT catalyst reported in Fig. 10 for comparison purpose. Also in this case, the oxidation of soot takes place progressively during the subsequent lean–rich cycles; however, the oxidation ability of the Pt-based catalyst is much lower than that of the CeO_2-based system, since in the latter case the participation of active oxygen species coming from CeO_2 and/or Ag sites improves the oxidizing performances of the catalytic system.

The behavior of Ag–Sr/CeO_2 catalyst in the presence of soot has also been tested and the results are reported in Fig. 8C (first cycle) and D (seventh cycle and TPO). The total amount of stored NO_x vs. cycle number is reported in Fig. 9B, while the conversion of soot during the lean phase as a function of the cycle number is shown in Fig. 10 (dotted line).

The results clearly show that the NO_x storage capacity of the Sr-containing catalyst decreases in the presence of soot; the NO_x breakthrough is still zero and the amount of stored NO_x is further decreased by the NO_x desorption at NO and O_2 shut off, so at the end of the first storage phase 1.15×10^{-4} mol/g_{cat} are present at catalyst surface (vs. 7.82×10^{-4} mol/g_{cat}). Moreover, the NO/NO_2 ratio changes from 3.88 in the first cycle to 2.65 in the seventh one, and it does not reach the initial value of 1.58 in the absence of soot. The detrimental effect of soot on the storage capacity of Ag–Sr/CeO_2 catalyst seems to be independent from the amount of residual soot, i.e. at the end of the seventh cycle the catalyst does not recover its original performance, when more than 60% of soot has been oxidized (see Fig. 10). Also the soot oxidation capability is lower than in case of Ag–Ba/CeO_2 catalyst; indeed, a soot conversion of 13% is observed in the first cycle increasing up to 74% in the seventh one. Accordingly, the combustion of soot is completed during the subsequent final TPO run.

Finally, the effect of soot on the storage capacity has been studied also in the case of Ag–Ba/ZrO_2 catalyst and the results in terms of stored NO_x vs. cycle number are reported in Fig. 9C. The behavior is qualitatively similar to that observed in the case of CeO_2-based catalysts; indeed, the amount of stored NO_x decreases in the presence of soot and the system partially recover the storage capacity exhibited in the absence of soot only when most of the soot present is burnt. On the other hand, the soot conversion reported in Fig. 10 is lower than that of Ag–Ba/CeO_2 at the beginning and increases up to 90% at the end of the lean–rich sequence.

4. Conclusions

The study focuses on the catalytic behavior of Ag-based catalysts in both soot oxidation and simultaneous removal of soot and NO_x. The results have been compared with that obtained on the reference Pt–Ba/Al_2O_3 LNT catalyst.

It has been found that all the Ag-containing catalysts are able to oxidize soot in the presence of NO/O_2 at temperatures near 250 °C, remarkably lower than the uncatalyzed soot oxidation; the presence of Ba or Sr does not significantly affect the catalytic activity. On the other hand, the Ag dispersion improves the oxidation activity, i.e. the catalyst with lower Ag dispersion exhibits higher onset oxidation temperature.

All the Ag-containing catalysts are able to simultaneously remove soot and NO_x, when operating under isothermal cycling conditions, i.e. alternating lean–rich phases according to the typical DPNR strategy. The data show that in the absence of soot the storage capacity of the investigated systems is higher than that of traditional Pt–Ba/Al_2O_3 LNT catalyst; however, in the presence of soot, the detrimental effect of soot on the storage capacity is more evident in the case of Ag-based catalysts. The latters are by far more active in the soot combustion than the Pt-based catalyst, possibly due to the participation of oxygen active species from ceria and/or silver.

In conclusion, the results point out that Ag-based catalysts should be considered as a promising alternative to Pt-based catalysts for the simultaneous removal of soot and NO_x. However, their reactivity in the reduction of the stored NO_x should be further enhanced to improve the N_2 selectivity.

Acknowledgments

The authors thank financial support from MIUR (Futuro in ricerca, FIRB 2012, project SOLYST). J. Llorca is grateful to ICREA Academia program.

References

[1] A. Russell, W.S. Epling, Catal. Rev. 53 (2011) 337–423.
[2] T.V. Johnson, Int. J. Engine Res. 10 (2009) 275–285.
[3] J.P.A. Neeft, M. Makkee, J.A. Moulijn, Fuel Process. Technol. 47 (1996) 1–69.
[4] B.A.A.L. van Setten, R. van Dijk, S.J. Jelles, M. Makkee, J.A. Moulijn, Appl. Catal. B: Environ. 21 (1999) 51–61.
[5] M.J. Maricq, Aerosol Sci. 38 (2007) 1079–1118.
[6] M.V. Twigg, Appl. Catal. B: Environ. 70 (2007) 2–15.
[7] D. Fino, V. Specchia, Powder Technol. 180 (2008) 64–73.
[8] J.P.A. Neeft, M. Makkee, J.A. Moulijn, Appl. Catal. B: Environ. 8 (1996) 57–78.
[9] N.K. Labhsetwara, M. Dhakada, S.S. Rayalua, R. Kumara, J. Subrtb, H. Hanedac, S. Devottaa, T. Mitsuhashi, Top. Catal. 42–43 (2007) 299–302.
[10] A.M. Hernández-Giménez, D. Lozano Castelló, A. Bueno-López, Chem. Pap. 68 (2014) 1154–1168.
[11] E. Aneggi, C. de Leitenburg, A. Trovarelli, Catalysis by Ceria and Related Materials, vol. 12, 2nd ed., Imperial College Press, 2013, pp. 565–621.
[12] A. Bueno-López, Appl. Catal. B: Environ. 146 (2014) 1–11.
[13] E. Aneggi, C. de Leitenburg, A. Trovarelli, Catal. Today 181 (2012) 108–115.
[14] M. Machida, Y. Murata, K. Kishikawa, D. Zhang, K. Ikeue, Chem. Mater. 20 (2008) 4489–4494.
[15] E. Aneggi, J. Llorca, C. de Leitenburg, G. Dolcetti, A. Trovarelli, Appl. Catal. B: Environ. 91 (2009) 489–498.
[16] C. Wen, A.Y. Yin, W.L. Dai, Appl. Catal. B: Environ. 160 (2014) 730–741.
[17] G. Preda, G. Pacchioni, Catal. Today 177 (2011) 31–38.
[18] K.-I. Shimizu, H. Kawachi, A. Satsuma, Appl. Catal. B: Environ. 96 (2010) 169–175.
[19] T. Nanba, S. Masukawa, A. Abe, J. Uchisawa, A. Obuchi, Catal. Sci. Technol. 2 (2012) 1961–1966.
[20] G. Corro, U. Pal, E. Ayala, E. Vidal, Catal. Today 212 (2013) 63–69.
[21] D. Reichert, H. Bockhorn, S. Kureti, Appl. Catal. B: Environ. 80 (2008) 248–259.
[22] K. Krishna, A. Bueno-López, M. Makkee, J.A. Moulijn, Appl. Catal. B: Environ. 75 (2007) 201–209.
[23] J. Suzuki, S. Matsumoto, Top. Catal. 28 (2004) 171–176.
[24] K. Nakatani, S. Hirota, S. Takeshima, K. Itoh, T. Tanaka, SAE Paper SP-1674, 2002-1-0957, 2002.
[25] R. Matarrese, L. Castoldi, L. Lietti, P. Forzatti, Top. Catal. 52 (2009) 2041–2046.
[26] N. Miyoshi, S. Matsumoto, K. Katoh, T. Tanaka, J. Harada, N. Takahashi, K. Yokota, M. Sugiura, K. Kasahara, SAE Tech. Pap. (1995) 950809.
[27] S. Matsumoto, Catal. Today 29 (1996) 43–45.
[28] N. Takahashi, H. Shinjoh, T. Iijima, T. Szuki, K. Yamazaki, K. Yokota, H. Suzuki, N. Miyoshi, S. Matsumoto, T. Tanizawa, T. Tanaka, S. Tateishi, K. Kasahara, Catal. Today 27 (1996) 63–69.
[29] H. Shinjoh, N. Takahashi, K. Yokota, M. Sugiura, Appl. Catal. B: Environ. 15 (1998) 189–201.
[30] L. Lietti, M. Daturi, V. Blasin-Aubé, G. Ghiotti, F. Prinetto, P. Forzatti, ChemCatChem 4 (2012) 55–58.
[31] L. Castoldi, R. Matarrese, L. Lietti, P. Forzatti, Appl. Catal. B: Environ. 64 (2006) 25–34.
[32] N. Artioli, R. Matarrese, L. Castoldi, L. Lietti, P. Forzatti, Catal. Today 169 (2011) 36–44.
[33] R. Matarrese, N. Artioli, L. Castoldi, L. Lietti, P. Forzatti, Catal. Today 184 (2012) 271–278.
[34] R. Matarrese, L. Castoldi, L. Lietti, P. Forzatti, Top. Catal. 42–43 (2007) 293–297.
[35] R. Matarrese, L. Lietti, L. Castoldi, G. Busca, P. Forzatti, Top. Catal. 56 (2013) 477–482.
[36] R. Matarrese, L. Castoldi, N. Artioli, E. Finocchio, G. Busca, L. Lietti, Appl. Catal. B: Environ. 144 (2014) 783–791.
[37] K. Krishna, M. Makkee, Catal. Today 114 (2006) 48–56.
[38] A. Setiabudi, M. Makkee, J.A. Moulijn, Appl. Catal. B: Environ. 50 (2004) 185–194.
[39] B.A.A.L. van Setten, M. Makkee, J.A. Moulijn, Catal. Rev. 43 (2001) 489–564.

[40] M.A. Peralta, M.S. Gross, B.S. Sanchez, C.A. Querini, Chem. Eng. J. 152 (2009) 234–241.
[41] L. Lietti, P. Forzatti, I. Nova, E. Tronconi, J. Catal. 204 (2001) 175–191.
[42] F. Frola, M. Manzoli, F. Prinetto, G. Ghiotti, L. Castoldi, L. Lietti, J. Phys. Chem. C 112 (2008) 12869–12878.
[43] C. Morterra, G. Magnacca, V. Bolis, G. Cerrato, M. Baricco, A. Giachello, M. Fucale, in: A. Frennet, J.-M. Bastin (Eds.), Catalysis and automotive pollution control III, Stud. Surf. Sci. Catal. 96 (1995) 361–373.
[44] A. Piras, A. Trovarelli, G. Dolcetti, Appl. Catal. B: Environ. 28 (2000) L77–L81.
[45] X.D. Wu, S.A. Liu, F. Lin, D.A. Weng, J. Hazard. Mater. 181 (2010) 722–728.
[46] C. Lei, M.Q. Shen, M. Yang, J. Wang, J. Wang, Appl. Catal. B: Environ. 101 (2011) 355–365.
[47] V.G. Milt, E.D. Banus, E.E. Miró, M. Yates, J.C. Martin, S.B. Rasmussen, P. Avila, Chem. Eng. J. 157 (2010) 530–538.
[48] T. Nanba, S. Masukawa, A. Abe, J. Uchisawa, A. Obuchi, Appl. Catal. B: Environ. 123 (2012) 351–356.
[49] F. Giordano, A. Trovarelli, C. de Leitenburg, M. Giona, J. Catal. 193 (2000) 273–282.
[50] L. Ilieva, J.W. Sobczak, M. Manzoli, B.L. Su, D. Andreeva, Appl. Catal. A: Gen. 291 (2005) 85–92.
[51] E.P. Reddy, R.S. Varma, J. Catal. 221 (2004) 93–101.
[52] Z.P. Qu, M.J. Cheng, W.X. Huang, X.H. Bao, J. Catal. 229 (2005) 446–458.
[53] N. Gungor, S. Isci, E. Gunister, W. Mista, H. Teterycz, R. Klimkiewicz, Appl. Clay Sci. 32 (2006) 291–296.
[54] Z.P. Qu, M.J. Cheng, X.L. Dong, X.H. Bao, Catal. Today 93–95 (2004) 247–255.
[55] G.I.N. Waterhouse, G.A. Bowmaker, J.B. Metson, Appl. Surf. Sci. 214 (2003) 36–51.
[56] A.J. Nagy, G. Mestl, D. Herein, G. Weinberg, E. Kitzelmann, F. Schlogl, J. Catal. 182 (1999) 417–429.
[57] L. Kundakovic, M. Flytzani-Stephanopoulos, Appl. Catal. A: Gen. 183 (1999) 35–51.
[58] M. Machida, Y. Murata, K. Kishikawa, D.J. Zhang, K. Ikeue, Chem. Mater. 20 (2008) 4489–4494.
[59] J. Oi-Uchisawa, A. Obuchi, R. Enomoto, J.Y. Xu, T. Nanba, S.T. Liu, S. Kushiyama, Appl. Catal. B: Environ. 32 (2001) 257–268.
[60] B.J. Cooper, S.A. Roth, Platin. Met. Rev. 35 (1991) 178–187.
[61] L. Castoldi, I. Nova, L. Lietti, P. Forzatti, Catal. Today 96 (2004) 43–52.
[62] I. Nova, L. Castoldi, L. Lietti, E. Tronconi, P. Forzatti, F. Prinetto, G. Ghiotti, J. Catal. 222 (2004) 377–388.
[63] W.S. Epling, L.E. Campbell, A. Yezerets, N.W. Currier, J.E. Parks II, Catal. Rev. 46 (2004) 163–245.
[64] I. Nova, L. Castoldi, L. Lietti, E. Tronconi, P. Forzatti, Top. Catal. 42–43 (2007) 21–25.
[65] J.A. Sullivan, O. Keane, A. Cassidy, Appl. Catal. B: Environ. 75 (2007) 102–106.
[66] L. Castoldi, N. Artioli, R. Matarrese, L. Lietti, P. Forzatti, Catal. Today 157 (2010) 384–389.
[67] S.J. Jelles, R.R. Krul, M. Makkee, J.A. Moulijn, Catal. Today 53 (1999) 623–630.